Flexible Hybrid Electronics: Direct Interfacing of Soft and Hard Electronics for Wearable Health Monitoring

17 authors, including:

Yasser Khan
Stanford University
40 PUBLICATIONS   **2,159** CITATIONS

SEE PROFILE

Qiong Gui
Binghamton University
16 PUBLICATIONS   **465** CITATIONS

SEE PROFILE

Abhinav Gaikwad
Moses Lake Industries, Portland
28 PUBLICATIONS   **1,438** CITATIONS

SEE PROFILE

Natasha Ariane Diniz Yamamoto
University of California, Berkeley
20 PUBLICATIONS   **348** CITATIONS

SEE PROFILE

Some of the authors of this publication are also working on these related projects:

Project   Flexible biophotonic sensors View project

Project   Flexible Hybrid Electronics View project

Flexible Hybrid Electronics: Direct Interfacing of Soft and Hard Electronics for Wearable Health Monitoring

Yasser Khan, Mohit Garg, Qiong Gui, Mark Schadt, Abhinav Gaikwad, Donggeon Han, Natasha A. D. Yamamoto, Paul Hart, Robert Welte, William Wilson, Steve Czarnecki, Mark Poliks, Zhanpeng Jin, Kanad Ghose, Frank Egitto, James Turner, and Ana C. Arias*

The interfacing of soft and hard electronics is a key challenge for flexible hybrid electronics. Currently, a multisubstrate approach is employed, where soft and hard devices are fabricated or assembled on separate substrates, and bonded or interfaced using connectors; this hinders the flexibility of the device and is prone to interconnect issues. Here, a single substrate interfacing approach is reported, where soft devices, i.e., sensors, are directly printed on Kapton polyimide substrates that are widely used for fabricating flexible printed circuit boards (FPCBs). Utilizing a process flow compatible with the FPCB assembly process, a wearable sensor patch is fabricated composed of inkjet-printed gold electrocardiography (ECG) electrodes and a stencil-printed nickel oxide thermistor. The ECG electrodes provide 1 mVp–p ECG signal at 4.7 cm electrode spacing and the thermistor is highly sensitive at normal body temperatures, and demonstrates temperature coefficient, $\alpha \approx -5.84$ K^{-1} and material constant, $\beta \approx 4330$ K. This sensor platform can be extended to a more sophisticated multisensor platform where sensors fabricated using solution processable functional inks can be interfaced to hard electronics for health and performance monitoring, as well as internet of things applications.

1. Introduction

Recent thrust toward wearable medical devices has encouraged a myriad of efficient skin-like sensors that are extremely promising for medical monitoring,[1–7] imaging,[8] and diagnostics.[9] The soft form factor of these sensors allows pristine sensor interfaces to human skin, which significantly improves the signal-to-noise ratio.[8–10] In addition, these sensors are configurable and can be fabricated in different sizes and shapes that better suit the diverse human population. However, these flexible sensors require rigid silicon-based integrated circuits (ICs) for data processing and communications.[11–13] Although the tremendous mechanical mismatch of hard electronics and the soft human skin hinders sensor–skin interface, silicon ICs provide unparalleled computational performance at lower power than their flexible counterparts based on organic/inorganic materials.[14,15] Therefore, a hybrid solution with soft and hard electronics is well suited, where flexible devices are used for soft biointerfaces and hard electronics are used for computation, signal processing, and data transmission.

Printed sensors provide a distinct advantage over rigid sensors at establishing high-fidelity sensor–skin interfaces due to their inherently flexible material systems and form factors. Hence, these sensors are suitable for monitoring vital signs as well as analytes in bodily fluids.[16–18] Flexible hybrid electronics (FHE) are a fundamental enabling technology for system-level implementation of these novel printed and flexible devices. FHE bring together soft and hard electronics into a single platform, where the soft devices are used for conformal

Y. Khan, Dr. A. Gaikwad, Dr. D. Han, Dr. N. A. D. Yamamoto, Prof. A. C. Arias
Department of Electrical Engineering and Computer Sciences
University of California
Berkeley, CA 94720, USA
E-mail: acarias@eecs.berkeley.edu
M. Garg, Prof. K. Ghose
Department of Computer Science
Binghamton University
State University of New York
Binghamton, NY 13902, USA
Q. Gui, Prof. Z. Jin
Department of Electrical and Computer Engineering
Binghamton University
State University of New York
Binghamton, NY 13902, USA

Dr. M. Schadt, P. Hart, W. Wilson, F. Egitto
i3 Electronics, Inc.
Endicott, NY 13760, USA
R. Welte
ExSys Technology, Inc.
Endicott, NY 13760, USA
Dr. S. Czarnecki, Prof. M. Poliks, Dr. J. Turner
Small Scale Systems Integration & Packaging Center
Binghamton University
State University of New York
Binghamton, NY 13902, USA

FULL PAPER

sensor interfaces, and the hard silicon-based devices provide the computational backbone and compatibility with existing electronic systems and standards. FHE comprise (1) soft sensors or devices for conformal interfaces, (2) hard silicon-based electronics for computations, (3) interface between the soft and hard electronics, and (4) power source and driver electronics.[19,20] Since soft electronics use novel materials and substrates, a multitude of deposition techniques is used for fabricating these devices.[21,22] Therefore, integrating devices, sensors, and ICs fabricated using vastly dissimilar technologies is a key challenge for FHE. Currently, a multisubstrate approach is employed where sensors and devices are fabricated on one flexible substrate, and then, interfaced to another flexible printed circuit board (FPCB) that hosts the rigid electronics using bonding or connectors.[5,9,23] This approach of interfacing is prone to alignment and interconnect issues.

In this work, we report on an interfacing scheme, where sensors are directly printed on flexible Kapton polyimide (PI) substrate that hosts the silicon ICs and rigid passive components. This fabrication flow is completely compatible with the assembly-line process utilized in the FPCB industry and minimizes interconnect complexities. Using the direct printing technique, we fabricated a wearable sensor patch (WSP) capable of measuring electrocardiography (ECG) signal and skin temperature. The ECG electrodes are inkjet printed using gold nanoparticle ink. Since the surface energy of bare Kapton PI is not optimized for inkjet printing, we employed a series of surface energy modifications using tetrafluoromethane (CF_4) and oxygen (O_2) plasma. After the plasma treatments, we achieved high-quality inkjet-printed electrodes, which are reproducible and robust. The thermistor is fabricated by stencil-printing nickel oxide (NiO) nanoparticle ink. The thermistor demonstrates temperature coefficient, $\alpha \approx -5.84\%$ K^{-1} and material constant, $\beta \approx 4330$ K. Moreover, the sensitivity range of the thermistor covers the normal human skin temperature range of 32–37 °C. We anticipate that our results can be extended to a more sophisticated multisensor platform where sensors fabricated using other solution processable functional inks can be interfaced to hard electronics for health and performance monitoring, as well as internet of things applications.

2. Results and Discussion

2.1. Wearable Sensor Patch

The proposed WSP shown in **Figure 1**a is an example of FHE implementation, where sensors fabricated by printing techniques are integrated with conventional electronics into a flexible sensing platform. The sensor patch utilizes a pair of printed gold electrodes for sensing ECG signal and a printed nickel oxide thermistor for measuring skin temperature. The complete system is being assembled on a Kapton PI substrate, where the printed sensors are interfaced to silicon ICs, i.e., an analog front end (AFE), a Bluetooth System on Chip (SoC), and other hard passive components.

The WSP is being fabricated and assembled on a 5.08 cm × 5.08 cm, 50 µm thick flexible Kapton PI substrate as shown in Figure 1b. The area is chosen to balance the need for a large

ECG electrode spacing with the desire to minimize area for wearer's comfort. This dimension ensures the wearable form factor and allows 4.7 cm spacing between the ECG electrodes. Gold-printed electrodes are used for acquiring the ECG signal. An AFE amplifies and filters the signal before sending to a host computer via Bluetooth SoC. Filtering and amplifying can also be done using discrete components in conjunction with the Bluetooth SoC; however, the AFE approach reduces the number of required discrete components. The skin temperature is recorded using a stencil-printed nickel oxide, negative temperature coefficient (NTC) thermistor. The thermistor is used in a voltage divider network, where the voltage across the thermistor varies according to the temperature, which is digitized and recorded using an analog-to-digital converter (ADC) of the Bluetooth SoC. The complete system is powered by a coin cell battery of 220 mAh capacity. Although flexible thin-film batteries were considered, the capacity requirement of the battery proved challenging for the thin-film batteries. Additionally, the patch is intended for disposable use; therefore, a coin cell battery was chosen over rechargeable thin-film batteries. Since the WSP is currently being developed, the thermistor data presented in this paper are from discrete devices and the ECG data are collected from a fully assembled WSP. Design challenges, further optimizations, as well as simultaneous recording from the sensors will be reported in a subsequent paper.

2.2. Single-Substrate Integration by Direct Printing of Sensors on Kapton PI Substrate

The substrates conventionally used in printed electronics such as polyethylene terephthalate (PET) and polyethylene naphthalate (PEN) deform and melt at temperatures over 200 °C. However, FPCB process flow commonly requires processing temperature over 200 °C for electronic component assembly via solder reflow. Consequently, for integrating printed electronics to FPCBs, printed devices are typically processed on PET or PEN, and then attached to FPCBs using a low-temperature bonding process or by connectors. On the contrary, we employ a single-substrate approach and fabricate the WSP on a single Kapton PI substrate with the printed sensors on one side and attach the electronic components on the other side. This approach simplifies the manufacturing protocol by using a single substrate, and obviates the bonding process that may not form a robust connection in the final device.

2.3. Inkjet-Printed Gold ECG Electrodes

The surface energy of Kapton PI that is used for FPCB is significantly higher than what is required for inkjet printing (IJP). Therefore, IJP on Kapton PI is challenging. During IJP, the nanoparticle ink experiences both cohesion and adhesion forces on the substrate (Figure S1, Supporting Information). These forces equilibrate and the contact angle (θ) between the droplet and the substrate provides an inverse relation to the surface energy of the substrate. To obtain reliable inkjet-printed features, appropriate surface energy is crucial.
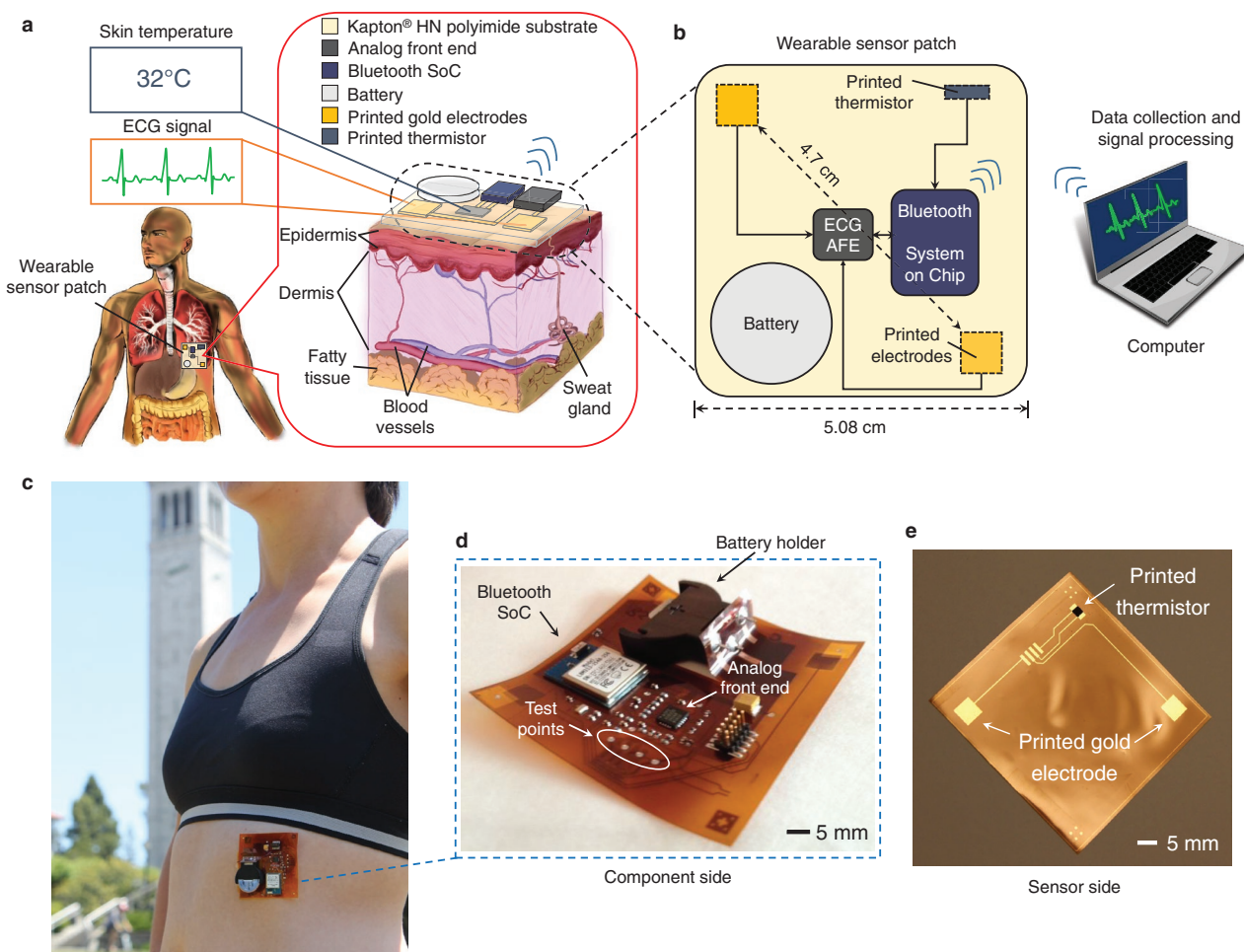
www.MaterialsViews.com

ADVANCED
FUNCTIONAL
MATERIALS
www.afm-journal.de

FULL PAPER

Figure 1. Proposed overview and system design of the wearable sensor patch (WSP) enabled by flexible hybrid electronics. a) Schematic of the sensor patch placed on a subject's lower left rib cage. Skin temperature is read using a stencil-printed thermistor while the electrocardiography (ECG) signal is acquired using inkjet-printed gold electrodes. The electrodes and the thermistor are interfaced to silicon-based ICs for data acquisition, processing, and transmission. b) System design of the sensor patch. The ECG signal is obtained using an analog front end (AFE). The data are then processed and transmitted using a Bluetooth System on Chip (SoC) to a host computer. The thermistor data are read using a voltage divider network, where the voltage drop across the thermistor is sensed using an analog to digital converter (ADC) of the SoC. After data transmission, both ECG and thermistor data are displayed on a host computer. c) Photograph of the WSP mounted on a person's lower left rib cage. The sensor side faces down toward the skin, and the component side faces up. d) Photograph of the component side of the patch. The battery holder, the Bluetooth SoC, AFE, and the test points are shown. Reproduced with permission.[28] Copyright 2016, IEEE. e) Photograph of the sensor side of the patch (before component assembly). The printed gold ECG electrodes and the thermistor are shown.

Untreated Kapton PI shows a contact angle in the range of 45°–55° (**Figure 2**a). Contact angles lower than 70° cause the ink to spread as schematically shown in the printing tests of Figure 2a—the printed ink spreads at impact, and continues to spread further as shown in the micrographs at $t = 0$ and 60 s. To bring the surface energy down to a printable range, we treated the Kapton PI surface with CF_4 plasma. This treatment lowers the Kapton PI surface energy substantially as evidenced by the large increase in contact angle to over 90° (Figure 2b). However, with this low surface energy, ink–substrate adhesion forces are weaker than particle–particle cohesive forces. Hence, printed ink rapidly dewets from the surface as shown schematically and with optical micrographs in Figure 2b. A pad and an angled trace are printed, but the ink pulls back from the initial drop location and results in broken printed circuit traces.

Therefore, forming the intended features becomes increasingly difficult. A second treatment step with an O_2 plasma increases surface energy to bring the contact angle into the printable zone. Figure 2c shows contact angles in the range of 80°–88°. The surface energy associated with this contact angle has been found to be ideal for inkjet printing of our gold nanoparticle ink. We obtained high-quality printed pads and traces with complex bends using the CF_4 and O_2 plasma treatments. The prints show good feature definitions, and these optimization steps are used for printing the ECG electrodes of the WSP. Although it is possible to use only CF_4 plasma for the surface energy optimization, CF_4 plasma did not allow sufficient control to reproducibly tune the surface energy. Therefore, O_2 plasma is used in conjunction with CF_4 plasma for finer control and higher reproducibility to adjust the surface energy.
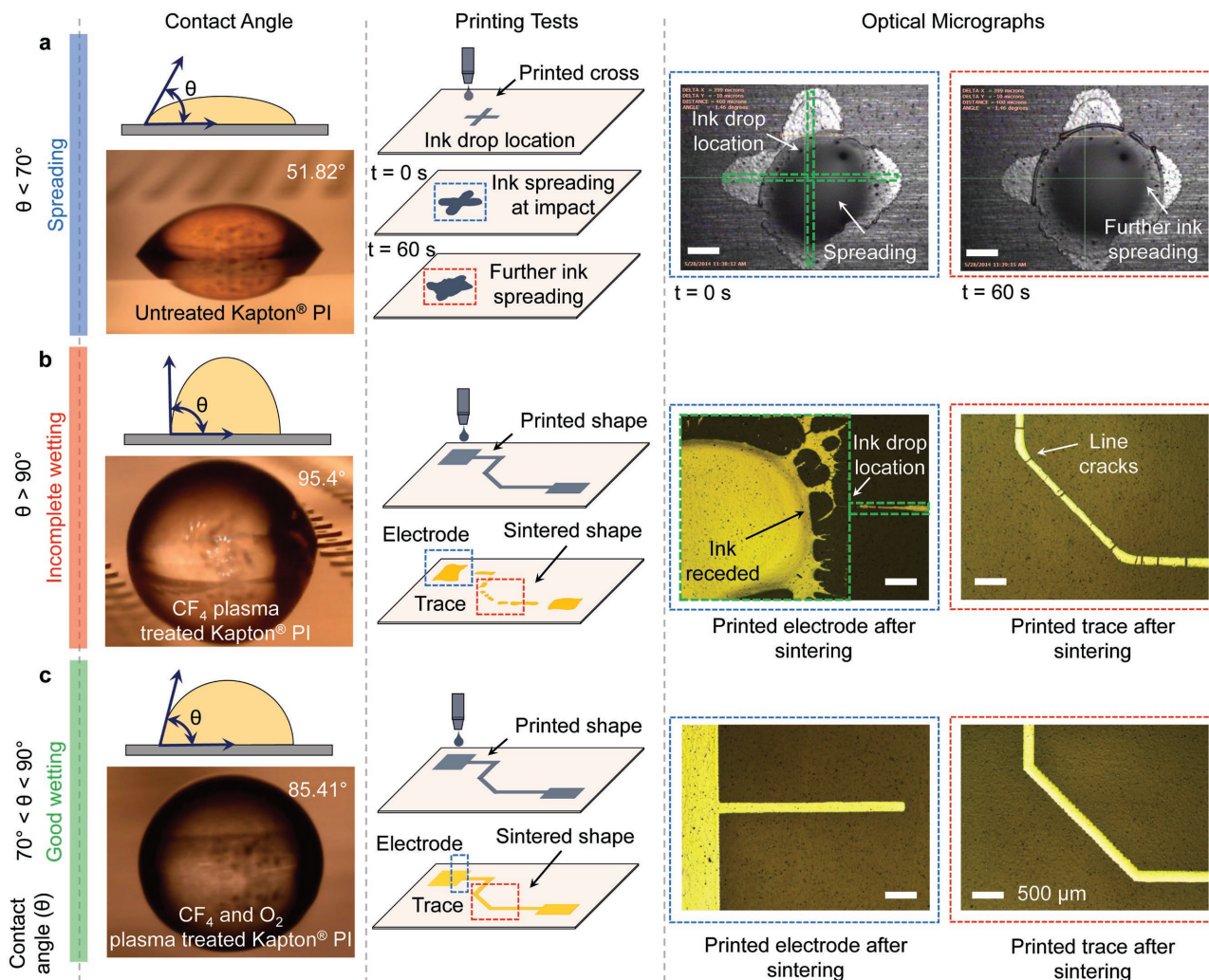
Figure 2. Surface energy optimizations for inkjet printing functional inks on Kapton PI substrate. Blue, red, and green colored rows show deionized (DI) water contact angle (θ) schematically and obtained from a goniometer, inkjet printing trials, and optical micrographs of printed structures on Kapton PI surfaces that show ink spreading, incomplete wetting, and good wetting, respectively. The scale bars in the micrographs represent 500 μm. a) Printing tests on untreated Kapton PI that shows uncontrolled spreading of ink. The high surface energy of untreated Kapton PI generates a contact angle less than 70°, which results in ink spreading as shown in the schematic of the "printed cross" and spreading of the ink (middle panel). The cross does not hold shape at impact, and the ink spreads further as shown by the micrograph that is taken 60 s after printing (right panel). b) Printing tests on CF_4 plasma treated Kapton PI that shows incomplete wetting of printed ink. To reduce the surface energy, the surface was fluorinated with CF_4 plasma treatment; hence, the contact angle goes above 90°. At this high contact angle, the printed ink recedes due to high cohesive forces within the ink, resulting in agglomeration of ink and dewetting clusters. The middle panel shows the schematic of a printed pad and an angled trace. Ink dewetting and line cracking are observed after sintering the gold nanoparticle ink. Micrographs of the pad and trace are shown in the right panel. Receding and agglomerating ink created discontinuities in the sintered shapes. c) Printing tests on CF_4 and O_2 plasma treated Kapton PI that shows good wetting of printed ink. After the O_2 plasma treatment, the contact angle comes down to the printable range, 70° < θ < 90°. In this case, high-quality printing is observed, as demonstrated by the micrographs of the printed pad and the angled trace in the right panel.

The electrical reproducibility of the printed gold electrodes is verified by using line and sheet resistance tests on electrodes of varying lengths. The length of electrodes e1, e2, e3, and e4 are 5.2, 3.7, 2.6, and 1.4 cm, respectively (electrodes e1 and e4 are shown in **Figure 3**a as an example). The line and sheet resistance are presented in Figure 3b using red and green bars, respectively. The mean line resistance of the electrodes goes down from 132 Ω in e1 to 47 Ω in e4, as the trace length is reduced. The mean sheet resistance varies from 0.26 Ω sq^{-1} in e1 to 0.32 Ω sq^{-1} in e4. The printed features demonstrate a conductivity of 7.14×10^6 S m^{-1}, which is 16% of gold's bulk

conductivity and agrees with our previous report on printed electrodes on PEN substrates.[10] The printing resolution is governed by the wetting of the printed ink on the substrate. For the combination of our printed gold ink and the plasma-treated Kapton PI substrate, we obtain 70 μm resolution as shown in Figure S2 (Supporting Information).

In our direct interfacing approach, the sensors are connected to the hard electronics by printing on top of the plated metal pads. Therefore, the interface between the printed gold and gold-plated copper pad as shown in Figure 3c needs to be electrically and mechanically pristine. Although both bare copper
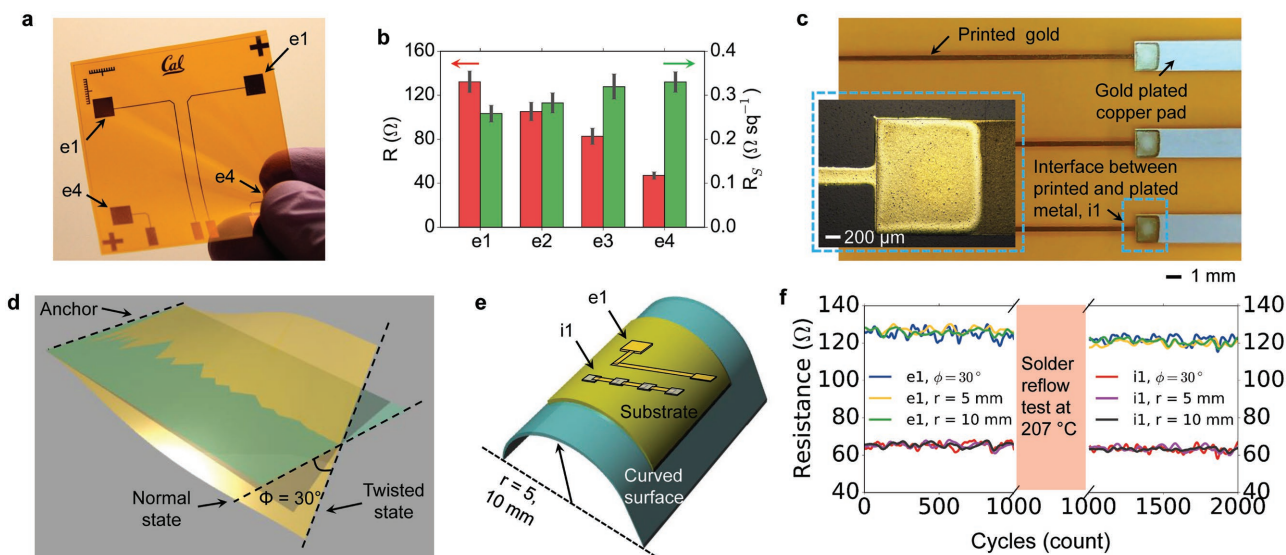
www.MaterialsViews.com

ADVANCED
FUNCTIONAL
MATERIALS
www.afm-journal.de

FULL PAPER

Figure 3. Electrical reproducibility and mechanical robustness testing of electrodes printed on Kapton PI and the interface between the printed gold and gold-plated copper pad. a) Photograph of printed electrodes of varying trace lengths. Four different trace lengths are used that are indicated by e1, e2, e3, and e4 (e1 and e4 are shown in the photograph as an example). b) Line (R) and sheet resistance (R_S) of the electrodes (the bar chart data are collected from 10 electrodes of the same length; the error bars represent the standard deviation of the data). c) Photograph of the interface between the printed gold and gold-plated copper pad. The blue inset shows a micrograph of the interface. d) Schematic illustration of the torsion testing setup. The printed device is anchored at two ends; the other two ends are twisted in opposing directions. Twist angle of $\varphi = 30°$ is used for the twist cycles. e) Schematic illustration of the bend testing setup. The printed devices are subjected to bending radii of 10 and 5 mm. f) Mechanical robustness testing results. The resistance of a printed trace (e1) that is bent to 10 mm (green) and 5 mm (yellow) bending radii, and twisted to 30° twist angle (blue). Similarly, the resistance of a line consisting of six printed/plated gold interfaces (i1) that is bent to 10 mm (black) and 5 mm (purple) bending radii, and twisted to 30° twist angle (red). The first 1000 cycles of bending and twisting are done before the solder reflow test, then the printed devices are run through a solder reflow oven at 207 °C. The second 1000 cycles of bending and twisting are done after the solder reflow test. Noise in resistance measurements arose from instrumentation and wire-pad contact resistance variations.

and gold-plated copper can be used on the FPCB side, oxidation of copper negatively impacts the contact. Since gold-plated copper pads do not suffer from oxidation, they provide a much cleaner interface for the printed gold.

The mechanical robustness of the printed lines and the interfaces is another key concern because the WSP needs to survive flexural wear and tear experienced when worn by a human. Therefore, to test the mechanical robustness, we torsionally loaded sensors with a 30° angle of twist (φ) and subjected to bending radii of 10 and 5 mm. The schematic in Figure 3d shows the conventions used in the twisting test—two ends of the substrate are anchored while the other two ends are twisted in opposing directions. Similarly, the schematic in Figure 3e shows the conventions used for the bend testing. The printed electrode (e1) and the interface (line consisting of six printed/plated gold interfaces, i1) are mechanically cycled for 2000 cycles and negligible change in the electrical resistance is observed (Figure 3f). At the very end of the manufacturing flow of the WSP, a solder reflow step is done, where the assembled sensor platform is subjected to a temperature profile, shown in the Figure S3 (Supporting Information), with a maximum of 207 °C, and the process is discussed in Section 2.5. Hence, we performed the bend and twist testing before and after a simulated solder reflow step to gauge the effect of high temperature of the fabrication flow. The electrical and mechanical properties of the printed traces remained intact after the solder reflow test, as seen by the negligible change in electrical resistance of the traces under test. Thus, our processes for ECG electrodes

and interconnects are reproducible and robust, i.e., the printed electrodes and traces can be fabricated with adequate precision and sufficiently low resistance (50–150 Ω), so that they will neither affect the ECG waveforms nor will they impact the circuit design.

2.4. Stencil-Printed Nickel Oxide Thermistors

The material system used for the thermistor is composed of NiO nanoparticles mixed with a polystyrene–butadiene rubber (PSBR) binder. In a thermistor formed by NiO and PSBR, the number of charge carriers in the conduction band of NiO increases with increasing temperature, resulting in a decrease in the resistivity, while PSBR holds the nanoparticles to form the thermistor. Since PSBR is viscid, stencil printing is chosen over inkjet printing. We fabricated the thermistors by stencil printing the NiO/PSBR composite on top of gold electrodes. An array of fabricated thermistors on Kapton PI substrates is shown in **Figure 4**a. The optimized ink demonstrates strong adhesion to the substrate, which is verified using the standard tape test. Optical and scanning electron microscope images of the printed thermistor are provided in Figure S4 (Supporting Information).

For reliably measuring human body temperature, good temperature sensitivity from 32 to 42 °C is extremely important. The resistance versus temperature plot is shown in Figure 4b. We observed high sensitivity at normal human body
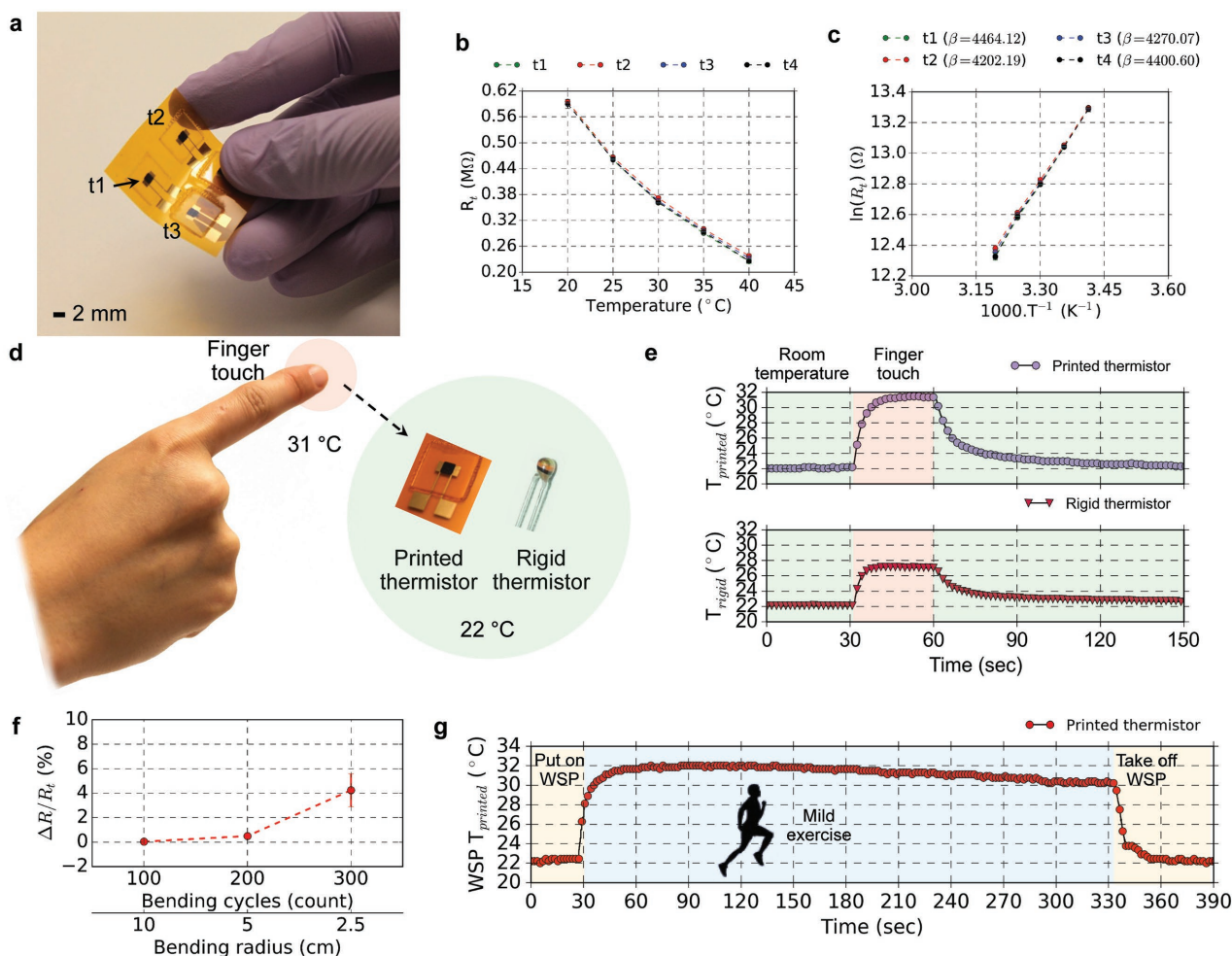
ADVANCED
FUNCTIONAL
MATERIALS
www.afm-journal.de

Materials
Views
www.MaterialsViews.com

Figure 4. Characterization and dynamic testing of the stencil-printed thermistors. a) Photograph of stencil-printed thermistors composed of nickel oxide (NiO) nanoparticles and PSBR binder on Kapton PI substrate. The four thermistors are labeled t1, t2, t3, and t4. b) Resistance versus temperature plot for the thermistors. c) β plot of the printed thermistors. d) Characterization of the dynamic response of the printed thermistor. The printed thermistor and a commercial rigid thermistor are used to study the dynamic response. Both thermistors are touched with an index finger to record the change in temperature (22–31 °C). e) The top panel shows the temperature read by the flexible thermistor and the bottom panel shows the temperature read by the rigid device. At normal condition (green), both thermistors show 22 °C, after touching the thermistors (red), the resistance drops due to the rise in temperature. As a result, the printed thermistor shows 31 °C, and the rigid thermistor shows 27 °C. f) Durability testing of the printed thermistors. Bending radii of 10, 5, and 2.5 cm are used, and the thermistors are subjected to 100 bending cycles at every bending radius. The room temperature resistance of the thermistors roughly changed by 0%, 0.5%, and 4%, respectively (the error bars represent data collected from eight devices). g) Real-time temperature monitoring using the thermistor. The thermistor accurately measured skin temperature of 30–32 °C during the exercise (blue overlay).

temperatures. The resistance at 30 °C ($R_{t@30}$) of the thermistors depends on the geometry of the thermistors. Our initial design, which had an 800 µm electrode gap underneath the thermistor, resulted in thermistors with $R_{t@30} > 5$ MΩ. However, to use the thermistors in the WSP, the $R_{t@30}$ of the thermistors needs to be a few hundred KΩ to a MΩ, for reliable operation of the thermistor circuitry. We reduced the $R_{t@30}$ of the thermistors by decreasing the electrode gap underneath the thermistor. The thermistors shown in Figure 4a have the dimensions of width 2 mm, length 2 mm, electrode gap 80 µm, and thickness 40 µm. This configuration resulted in an $R_{t@30}$ in the range of 350–375 kΩ (Figure 4b). For thermistors, beta (β), the slope of the graph in Figure 4c, is the measure of temperature sensitivity. Higher β will result in a greater change in resistance with

temperature change. We obtained $\beta \approx 4330$ K, which is comparable to $\beta \approx 4300$ K for inkjet-printed NiO thermistors reported by Huang et al.[24]

The change in resistance of the thermistor is governed by the general equation given below

$$R_t = R_0 \exp \beta \left(\frac{1}{T} - \frac{1}{T_0} \right) \tag{1}$$

Here, the resistance of the thermistor decreases with temperature increase, hence, the sensor is NTC type. R_t is the resistance at temperature T, R_0 is the resistance at T_0 (reference temperature), and β is the material constant for the thermistor. If β is known, Equation (1) can be solved for the temperature T:

$$T = \frac{1}{\dfrac{\ln\left(\dfrac{R_t}{R_0}\right)}{\beta} + \dfrac{1}{T_0}} \quad (2)$$

The β for the thermistor can be calculated by rearranging Equation (1):

$$\ln R_t = \ln R_0 + \beta\left(\frac{1}{T} - \frac{1}{T_0}\right) \quad (3)$$

A linear relationship between $\ln(R_t)$ and $1/T$ can be established, and β represents the slope of the $\ln(R_t)$ versus $1/T$ plot, which is related to the Boltzmann relation (E/kT), where E is the bandgap of the thermistor material and k is the Boltzmann's constant. Generally, the sensitivity of the thermistor is quantified using β and the temperature coefficient of the thermistor, α, which can be found by differentiating Equation (1) with respect to T and dividing by R_t:

$$\alpha = \frac{1}{R_t}\frac{dR_t}{dT} = -\frac{\beta}{T^2}\left(\%K^{-1}\right) \quad (4)$$

Both β and α can be used to characterize the performance of the thermistor; β has the units of Kelvin while α represents the percentage change in resistance per degree Kelvin. For calibrating the thermistors, we experimentally obtained resistance values for different temperatures and calculated β using Equation (3). This β is used in Equation (2) for calculating temperatures from the thermistor resistances. The resistance of thermistors is read from a voltage divider network composed of the thermistor in series with a 660 kΩ resistor (R). The variable voltage from the thermistor (V_t) is recorded, which is related to the resistance of the thermistor (R_t) by the equation below (V_B is the bias voltage):

$$V_t = V_B \times \frac{R_t}{(R_t + R)} \quad (5)$$

We also performed dynamic testing of the thermistor and compared the performance to a commercially available thermistor. The thermal time constant (τ) is the time required for a thermistor to change 63.2% of the total difference between its initial and final body temperatures under a step function change in temperature. When subjected to a step function temperature change from 31 to 22 °C, we measured $\tau_{printed} = 10$ s compared to $\tau_{rigid} = 11$ s of the rigid thermistor (Figure 4e). Under dynamic conditions, both thermistors are used to sense skin temperature—the thermistors are touched with an index finger and the responses are recorded (Figure 4d,e). When the thermistors are touched, the temperature rises from 22 to 31 °C. Figure 4e shows the temperature read by the thermistors while testing. At normal condition, the resistances of the thermistors are high, which results in a high voltage drop across the thermistors; hence, 22 °C temperature is recorded (the green zone in the panels). When touched, the voltage across the thermistors is reduced, and 31 and 27 °C temperatures are recorded by the printed and rigid thermistors, respectively (the

red zone in the panels). The printed thermistor provides a more accurate temperature reading of the index finger (31 °C) than the rigid device (27 °C) by establishing a conformal sensor–skin interface.

The durability of the printed thermistors (in WSP form factor) is verified by subjecting the devices to bend testing. Bending radii of 10, 5, and 2.5 cm are used so that the WSP uniformly fits the curved surface (Figure 4f). The room temperature resistance of the thermistors roughly changed by 0%, 0.5%, and 4% when the devices are subjected to bending radii of 10, 5, and 2.5 cm. For real-time temperature monitoring, a volunteer's skin temperature is recorded using the WSP mounted on the lower left rib cage while doing mild exercise. The sensor accurately measured 30–32 °C during the exercise as shown in Figure 4g. The thermistor data are obtained using a voltage divider network, where the variable voltage across the thermistor is recorded using an ADC of a Bluetooth SoC. It is worth noting that the encapsulation of the thermistor is extremely important as it needs to provide an adequate barrier to reduce moisture intake, as well as to protect the thermistor from the later processing of the manufacturing run. Initially, we used poly(methyl methacrylate) as the encapsulant that failed during the copper oxide cleaning step (utilizing oxalic acid) of the fabrication flow. Therefore, the thermistor data presented here are from an individual sensor rather than the fully assembled device. Currently, we opted for an amorphous fluoropolymer (Cytop) encapsulation, which provides superior barrier properties against the oxalic acid cleaning step (the process is described in Section 2.5).

2.5. Fabrication Process for the WSP

The fabrication process for the WSP is designed to be completely compatible with the FPCB assembly process. The process flow defined to manufacture the WSP is shown in **Figure 5**. Isometric and cross-sectional views of the process steps are shown side by side, as well as photographs of the device. A double-sided copper circuitized substrate is used (Figure 5a,b), where the "component side" hosts silicon ICs and rigid passive components. The sensors are printed on the opposite side of the frame—i.e., the "sensor side." The two sides of the copper circuit layers are interconnected by plated-through holes to provide interconnection from the side to which electronic components are mounted to the side on which the ECG electrodes and the thermistor are printed. This "sensor side" will be in contact with the skin of the wearer.

As described before, untreated Kapton PI substrates are not suitable for IJP. Therefore, the substrate is CF_4 and O_2 plasma treated to adjust the surface energy for IJP. Gold nanoparticle ink is inkjet printed at 30 µm drop spacing to form the gold ECG electrodes (Figure 5c,d,i). Commonly, FPCBs are processed on frames, where the Kapton PI substrate is mounted on a frame and subsequent processing is done on the frame. The side of the frame where the substrate is mounted is flat, whereas the opposite side forms a cavity between the frame and the substrate. IJP is done on the flat side of the fabrication frame, and the components are assembled on the cavity side of the frame (frame photo and design layouts are shown in
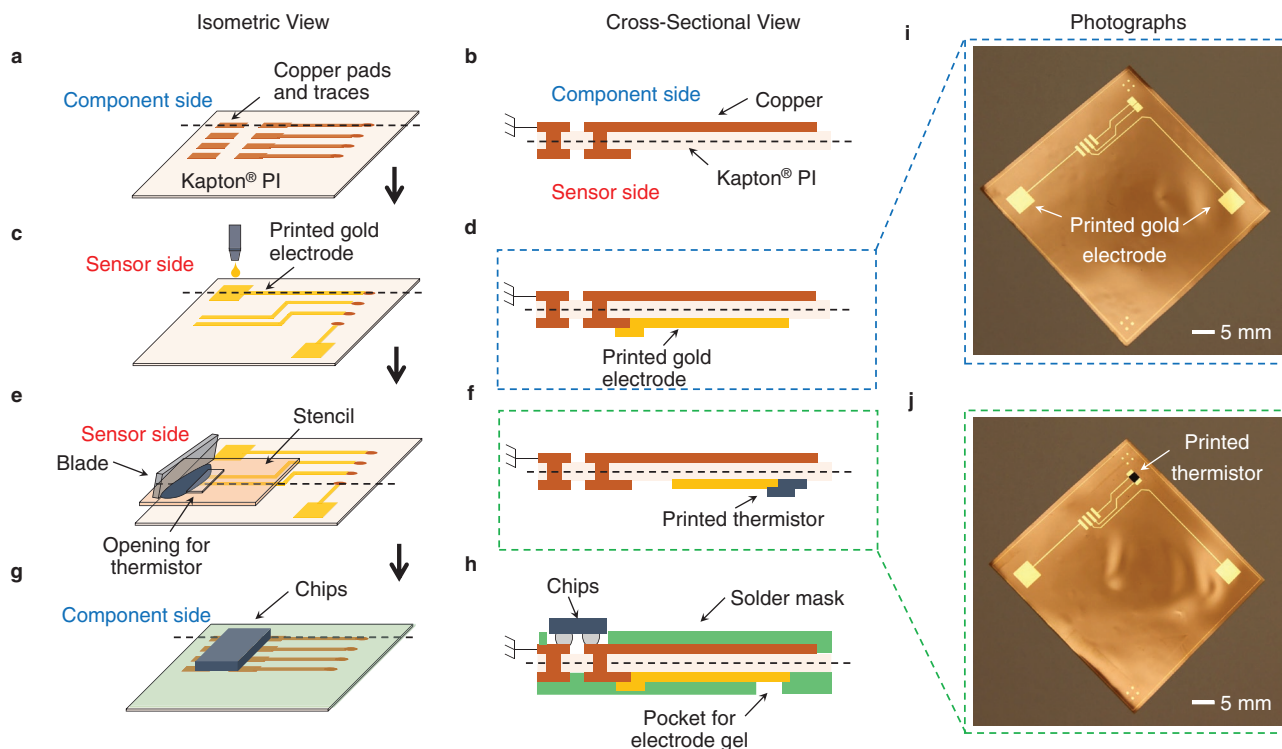
Figure 5. Fabrication process for the WSP. a–h) Simplified manufacturing steps illustrating the printing of gold electrodes and nickel oxide thermistors on Kapton PI substrate. a,c,e,g) Isometric views and b,d,f,h) corresponding cross-sectional views of the process steps are shown side by side. a,b) Standard double-sided copper circuitization is performed to deposit copper pads and traces. c,d) Gold nanoparticle ink is printed to fabricate the ECG electrodes and the electrodes for the thermistors. Surface energy optimization steps are performed before printing the gold ink. e,f) After sintering the gold ink, the thermistor is printed using stencil printing. The thermistor is printed on top of gold electrodes as seen in the cross-sectional view. g,h) After printing the sensors, photoimagebel solder mask process is executed keeping the electronic component pads and the ECG electrode pads open. The active and passive circuit components are soldered on the component pads through solder reflow. A pocket for the electrode gel is used, where electrode gel is applied before human measurement. i,j) Photographs of the printed gold electrodes (blue dotted box of part (d)) and nickel oxide thermistor (green dotted box of part (f)).

Figure S5 of the Supporting Information). Printed gold traces demonstrated a minimum linewidth of 70 μm. Since copper pads show higher surface energy, ink spreading is observed on the copper pads (Figure S6, Supporting Information). However, this turned out to be beneficial in the alignment process. To make electrical connection, gold traces are printed onto the surface of the copper pads. Since multiple connections are made side by side, the gold ink could not be allowed to flow between the tabs. The Kapton PI surface between the copper pads demonstrates relatively less surface energy; as a result, the ink is contained on the surface of the copper pads.

The thermistor is printed on top of gold electrodes using stencil printing (Figure 5e,f,j). A 50 μm PET stencil in conjunction with a glass slide as the blade are used to fabricate the thermistors. Thermistors of 2 mm length and width, and 40 μm height, are reproducibly printed that demonstrated 350–375 kΩ resistance at 30 °C. A Cytop encapsulation layer is applied on top of the thermistor to protect the device from the later processing steps as well as to reduce the moisture intake. The encapsulation process is shown in Figure S7 (Supporting Information).

Upon completion of the sensor build, the substrate is prepared for component assembly by solder mask deposition and laser cutting the coin cell battery holder. On the component side, the substrate is overcoated with a solder mask except for

select pads that are required for solder attach of components. On the sensor side, the substrate is also covered with solder mask leaving openings for the electrode pads for skin contact via a conductive gel. Finally, components are assembled via solder reflow, and electrode gel is applied to the opening of the ECG electrode before human testing. Photographs of the finished product are shown in Figure 1c–e.

2.6. Real-Time ECG Signal Monitoring with the WSP

Under clinical settings, ECG signal is measured using 10 electrodes placed around the body, 6 of which (V1–V6) are placed on the rib cage. This configuration is called 12-lead measurement, where the term "lead" refers to a view of the electrical activity of the heart from an angle across the body using a particular pair of electrodes.[25] In recording ECG signal, the printed gold electrodes provide 0.6 mVp–p signal compared to standard Ag/AgCl electrodes which provide 0.8 mVp–p signal when placed on the chest, V1–V2 chest lead placement locations (Figure S8, Supporting Information). Using the patch form factor, the WSP uses two electrodes to record the electrical signal. Here, the placement of the patch is of significant importance.

www.MaterialsViews.com

ADVANCED
FUNCTIONAL
MATERIALS
www.afm-journal.de

FULL PAPER

We used ECG signal magnitude and ease of securing the WSP as metrics for finding the suitable sensing location. Xu et al. used two electrodes mounted on the sternum and recorded ECG signal.[26] We obtained 0.6 mV signal magnitude using the same configuration. Although we tested multiple locations on the rib cage, the lower left rib cage area produced strong signals (green region in **Figure 6**a, starting from the fifth intercostal space). We used medical adhesive tape for securing the WSP to the skin. The complete assembly was 6.1 g, which was mostly dominated by the battery and the battery holder (3 and 2 g). Because of the flexible form factor and lightweight, the WSP remained secured to the skin during the wearer's physical movement. The electrodes diagonal to the WSP (yellow patch location in Figure 6a), aligned to the heart axis running from the upper right atrium through the lower left ventricle,

provided the strongest and cleanest ECG signal. High-quality and low-noise signals are recorded using these electrodes. We used this configuration for the ECG and heart rate (HR) variation measurements.

To test the efficacy of the WSP, we recorded ECG signal from human volunteers while at rest, and before, during and after mild exercise (Figure 6c–f). Figure 6c,d shows a snapshot of the raw ECG signal obtained from the hardware (from the blue overlay of Figure 6e). The different peaks of an ECG signal are labeled in Figure 6d. Figure 6e shows the filtered ECG signal for the complete test duration of 210 s; the red dots signify heartbeats detected by the peak detection algorithm. The raw signal is filtered to reduce noise in the higher frequencies that resulted in incorrect heartbeat peaks. The Fourier transform of the raw and filtered ECG signals is shown in Figure 6b. Noise
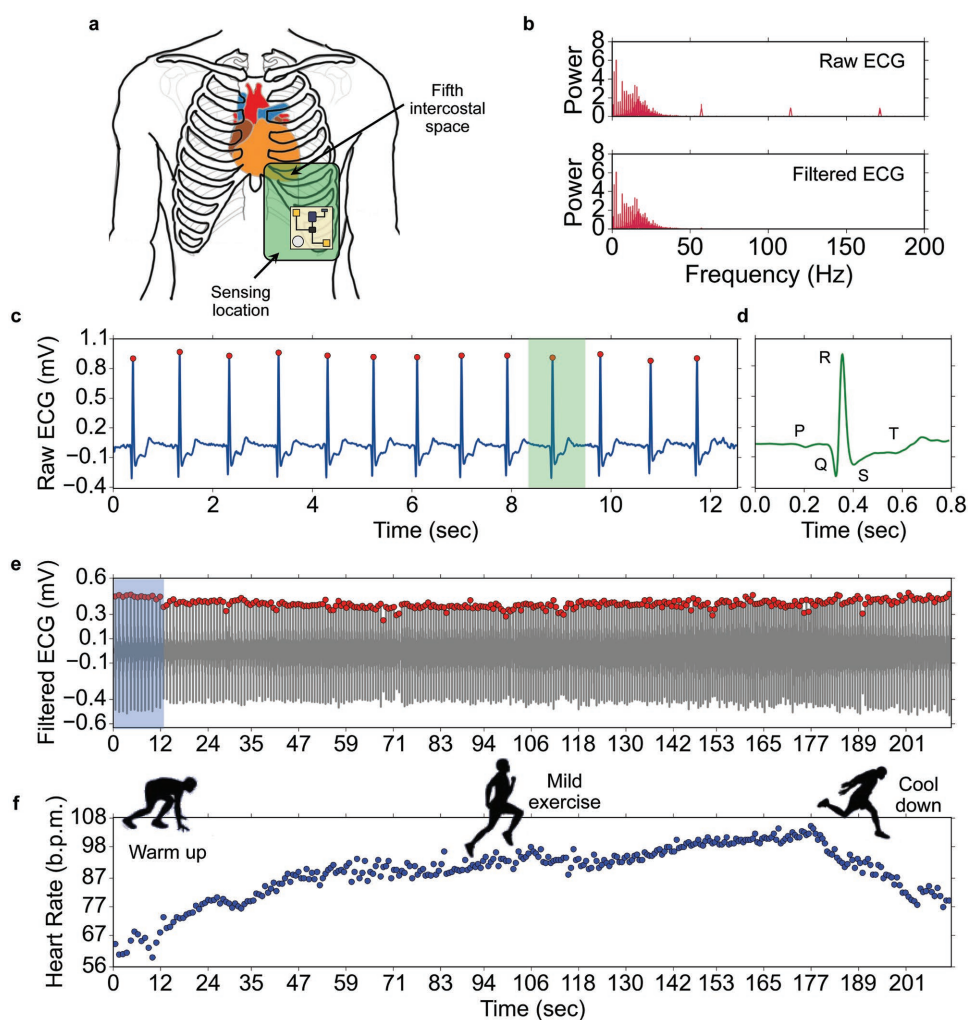

Figure 6. Electrocardiography (ECG) signal and heart rate (HR) monitoring using the WSP. a) Schematic illustration of the WSP placement on a subject's lower left rib cage. The region marked in green provides a low-noise and high-quality signal. Electrodes shown in the yellow patch are used to record the ECG signal during the mild exercise. b) Fourier transform of the raw and the filtered ECG signals. In the raw signal, noise at over 50 Hz hinders the peak detection algorithm. Therefore, a bandpass filter with 0.2 Hz (lower cutoff) and 45 Hz (upper cutoff) is used to filter the signal. c–f) ECG and HR from a subject while doing mild exercise. c) Raw ECG recording of the first 13 s. Data are taken from the blue overlay of the complete recording in part (e). The red dots signify heartbeats detected by the peak detection algorithm. d) A detailed view of the ECG signal collected from the green overlay in part (c) with marked P, Q, R, S, and T waveforms. e) The complete ECG recording (filtered) obtained during the time of exercise. Here also the red dots signify detected heartbeats. f) HR in beats per minute (b.p.m) for the complete duration of the exercise. Each blue dot is a representation of the time interval between two consecutive heartbeats.

**ADVANCED
FUNCTIONAL
MATERIALS**
www.afm-journal.de

*Materials
Views*
www.MaterialsViews.com

FULL PAPER

at over 50 Hz hinders the peak detection algorithm, resulting in errors in HR monitoring. After filtering the signal, the WSP clearly detected the heart rate variation during the mild exercise as shown in Figure 6f. HR of the volunteer picks up from the resting HR of 62 beats per minute (b.p.m.) to 108 b.p.m. after 3 min, and gradually cools down to 77 b.p.m. at the end of the recording. We obtained high-quality ECG signal from the WSP that was wirelessly transmitted to a computer host with essentially perfect peak detection. The HR showed anticipated variations corresponding to whether the subject was at rest or was exercising.

Motion artifacts are observed in the recordings, which are more prominent for dry electrodes. Using electrode gel significantly reduces motion artifacts and the associated noise. Additionally, the raw data are postprocessed to further reduce noise. An example recording with motion artifacts and noise at over 50 Hz is shown in **Figure 7**a. A detailed view of the ECG and the Fourier transform of the raw signal are shown in Figure 7b,c. Filtering the raw signal with a bandpass filter with 0.2 Hz (lower cutoff) and 45 Hz (upper cutoff) reduces most of the noise and eliminates all the incorrect heartbeat peaks (Figure 7d–f). However, some noise is still observed. Using a tighter filtering window further reduces noise; however, the ECG waveform is distorted because the filtering window cuts off frequencies associated with the ECG waveform as shown and discussed in Figure S9 (Supporting Information). Therefore, this filtering scheme is adequate for heart rate monitoring, but not suitable for recording medical-grade ECG signal.

Finally, to check the durability of the WSP, a 10 cm radius of curvature mandrel is used to bend test the complete WSP assembly as shown schematically in **Figure 8**a. Figure 8b,c shows the ECG recording from a simulator before the bend testing, and Figure 8d,e shows the ECG recording from the simulator after the bend testing. Here, the WSP is subjected to 200 cycles of bending. The WSP remained operational after the bending cycles. Although we observed some noise in the data, the signal was of an adequate quality for detecting the heart rate. This result indicates that the WSP platform remains functional after being subjected to mechanical bending; hence, this is suitable for wearable applications. Further design optimization in terms of thickness and shape of the printed and plated materials can be utilized to reduce corner stress concentration to further improve the mechanical robustness of the WSP.

Data related to mechanical testing presented in Figure 8 are obtained from a very small sampling of the first prototype WSP modules. A number of other modules, although functional prior to stressing, proved to be less robust upon mechanical stressing. The technology is sound, i.e., there are no issues stemming from electrical design, software, materials of construction, manufacturing methods, and workmanship. It is observed that failure to survive mechanical testing is due primarily to stress points in the device induced by the first pass physical design of the module, for example, circuit linewidths and routing, the size, shape, and location of openings in the solder mask layer to expose metal pads on the flexible substrate for component assembly. In addition, it is believed that changes in plated metal thickness, the thickness of the base Kapton PI substrate, and use of a gold surface finish on plated metals that interface with inkjet-printed gold will substantially improve module robustness. The design changes and other optimization to mitigate the adverse effect of these stress points are currently being investigated; this is beyond the scope of the present report, and will be described in a subsequent paper.

3. Conclusion

Battery lifetime of the WSP depends on the operation of the ECG AFE and the Bluetooth SoC communication protocols. The WSP operates cyclically in major and minor cycles. A major cycle has an active period followed by a quiescent period that can be of zero duration, i.e., absent. The main reason for operating in this mode is to conserve battery energy during the quiescent state, and collect and send periodic data to the
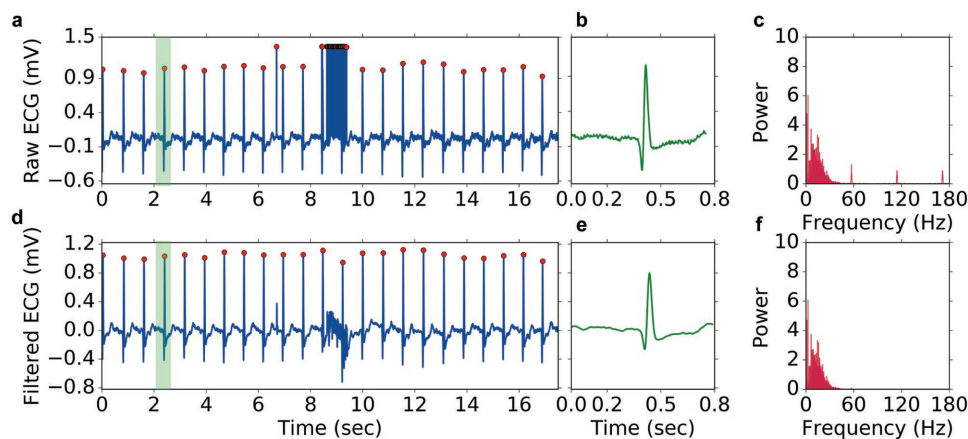

Figure 7. Post-processing of ECG signal for noise reduction. a–c) Raw ECG signal and corresponding signal features. a,b) Raw ECG signal and a detailed view of the signal for illustrating the ECG waveform (collected from the green overlay of the raw signal. The red dots signify detected heartbeats. c) Fourier transform of the signal, where motion artifacts and noise at over 50 Hz hinders the peak detection algorithm, resulting in errors in heart rate monitoring in part (a). d–f) Filtered ECG signal and corresponding signal features after filtering the raw signal with a bandpass filter with 0.2 Hz (lower cutoff) and 45 Hz (upper cutoff). Filtering reduces most of the noise and eliminates all the incorrect heartbeat peaks. However, some noise still remained as seen in part (d).
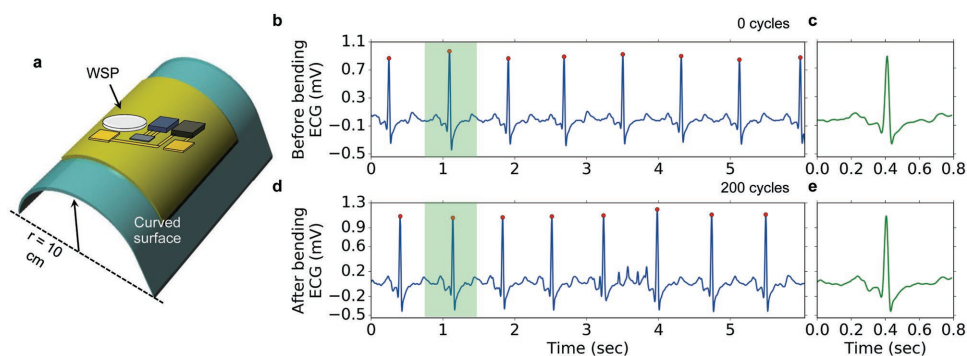
Figure 8. Mechanical robustness testing of the WSP. a) Schematic illustration of the bend testing setup where the WSP is subjected to mechanical bending using a 10 cm radius of curvature mandrel. b) ECG recording from a simulator before the bend testing. c) A detailed view of the recording taken from the green overlay region of part (b). d) ECG recording from the simulator after the WSP is subjected to 200 cycles of bending. e) A detailed view of the recording taken from the green overlay region of part (d).

host during the active period. Within a minor cycle, the WSP collects and buffers ECG signals and transmits the collected data. Running the WSP at full transmit power and 100% duty cycle provides a battery lifetime of 8 h. At a lower transmission power (–23 dBm) for the Bluetooth transmitter and a reduced duty cycle of 25%, we observed a drastic improvement of the lifetime to 38 h.

FHE brings together flexible sensors and silicon ICs under the same platform and utilizes these two different technologies at their strengths, i.e., flexible sensors for efficient biointerfaces and silicon ICs for computational purposes. However, interfacing flexible sensors to FPCBs is challenging due to bonding and alignment issues. Our integration scheme where both soft and hard electronics are hosted on one substrate significantly reduces fabrication complexities. Obviating the use of connectors significantly improves the flexibility of the device while keeping the connection integrity intact. Further optimization and improvement can be done on the WSP platform. For example, replacing the coin cell battery from the current design with a thin-film flexible battery would significantly enhance the flexibility of the device.[27] Moreover, integration of additional bioelectronic, biophotonic, and electrochemical sensors can take the application of this WSP platform beyond the fitness domain well into medical diagnostics. Our demonstration of direct integration of printed sensors to hard silicon ICs can serve as a stepping stone for a more sophisticated sensing platform where facile integration of novel solution-processable sensors to silicon ICs will unlock the true sensing capabilities of next-generation flexible sensors without hindering the flexibility and wearability of the device.

4. Experimental Section

Inkjet Printing and Characterization of ECG Electrodes: Untreated DuPont Kapton HN polyimide film used in FPCBs demonstrated higher than the required surface energy for inkjet printing; hence, a CF_4 plasma treatment step (March Plasma Systems C-7 series, 4000 W @ 40 kHz, total electrode plate area 44,594 cm^2, 100% power for 10 min at 0.24 mbar) and a subsequent O_2 plasma treatment step (Diener Nano, 300 W @ 40 kHz, total electrode plate area 2,520 cm^2, 24% power for 45 s at 0.24 mbar) were used to bring the surface energy into the printable zone. Then gold nanoparticle ink (Harima gold nanopaste ink

model: NPG-J) was printed using a Dimatix DMP 2800 inkjet printer with 30 µm drop spacing and 10 pL drops. An annealing step with 30 °C min^{-1} ramp from 30 to 230 °C and 1 h at 230 °C was used to fuse the nanoparticles yielding conductive lines and electrodes. Line and sheet resistance measurements of the electrodes were performed using a Keithley 2400 SourceMeter. The mechanical torsion testing was done using a custom setup where two ends of the device were anchored and the other two ends were twisted to an angle of 30°. The electrical resistance of the traces was recorded while twisting the devices for monitoring electrical and mechanical robustness.

Stencil Printing and Characterization of Thermistors: The thermistors were printed on top of the inkjet-printed gold electrodes using stencil printing. The thermistor was comprised of a 6:2:1 weight ratio of NiO (nickel(II) oxide nanopowder, <50 nm from Sigma-Aldrich), PSBR (Targray Technology), and deionized (DI) water. The ink was ball-milled overnight to create a well-mixed blend. The mixture was then printed using a 50 µm thick laser-cut PET stencil and a glass slide. Deposited film was cured for 2 h at 140 °C. Finished devices were encapsulated with 5 µm thick drop-casted Cytop fluoropolymer (CTX-809A). Thermistor layer thicknesses were measured with a Dektak profilometer. The temperature response of the thermistors was characterized on top of a custom-made hotplate by using a Keithley 2400 SourceMeter. The dynamic response of the thermistor was recorded using a voltage divider network composed of a thermistor in series with a 660 kΩ resistor—the variable voltage was recorded using an ADC of an Arduino Due board via universal asynchronous receiver/transmitter. The dynamic response of the printed thermistor was compared to a commercially available thermistor (Vishay NTCLE100E3103JB0).

Electronic Component Assembly: After printing the sensors, a cleaning step was performed to clean the copper oxide. Cascading rinses in 80 g L^{-1} oxalic acid solid in DI water for 2 min cleaned the copper oxide formed during the sintering step of the gold electrode fabrication. After that, the device was overcoated with photoimagable solder mask on both the sensor side and the component side leaving openings for the component pads and the ECG electrodes, where hydrogel (SignaGel Electrode Gel, Parker Laboratories, Inc.) was applied before taking ECG measurements. Then, components were assembled on top of the FPCBs and run through a solder reflow cycle to bond the ICs and passive components to the pads using tin 63: lead 37 solder.

WSP System Architecture for Sensor Data Acquisition, Processing, and Communication: At the core of the WSP was a Texas Instruments TI CC2540 SoC, which integrates a 12-bit ADC, a microcontroller, random access memory, flash memory, and peripherals along with a manageable, low-power Bluetooth transceiver. The CC2540 also features an analog multiplexer, which will be useful if the WSP is extended for additional sensors. Given the low signal levels from the ECG sensor on the patch and potential noise issues, a separate AFE ECG signal conditioning chip (AD8232) was used. The ECG signal was obtained using the AD8232,

ADVANCED
FUNCTIONAL
MATERIALS
www.afm-journal.de

Materials
Views
www.MaterialsViews.com

FULL PAPER

then, processed and transmitted using the CC2540 to a host computer. The thermistor read circuit consisted of a voltage divider network composed of the thermistor in series with a 660 kΩ resistor. All devices were operated by a single-ended DC source (coin cell of 220 mAh capacity and lithium chemistry). Human subject data were collected by placing the WSP on a volunteer's lower left rib cage; a host computer recorded the data transmitted by the WSP. The procedure was reviewed and approved by the Human Subjects Research Review Committee at Binghamton University (Protocol No. 3267-14).

Supporting Information

Supporting Information is available from the Wiley Online Library or from the author.

Acknowledgements

[1] T. Q. Trung, S. Ramasundaram, B.-U. Hwang, N.-E. Lee, *Adv. Mater.* **2016**, *28*, 502.

[2] S. Gong, W. Schwalb, Y. Wang, Y. Chen, Y. Tang, J. Si, B. Shirinzadeh, W. Cheng, *Nat. Commun.* **2014**, *5*, 3132.

[3] Y. Wang, L. Wang, T. Yang, X. Li, X. Zang, M. Zhu, K. Wang, D. Wu, H. Zhu, *Adv. Funct. Mater.* **2014**, *24*, 4666.

[4] C. M. Lochner, Y. Khan, A. Pierre, A. C. Arias, *Nat. Commun.* **2014**, *5*, 5745.

[5] W. Gao, S. Emaminejad, H. Y. Y. Nyein, S. Challa, K. Chen, A. Peck, H. M. Fahad, H. Ota, H. Shiraki, D. Kiriya, D.-H. Lien, G. A. Brooks, R. W. Davis, A. Javey, *Nature* **2016**, *529*, 509.

[6] T. Yokota, P. Zalar, M. Kaltenbrunner, H. Jinno, N. Matsuhisa, H. Kitanosako, Y. Tachibana, W. Yukita, M. Koizumi, T. Someya, *Sci. Adv.* **2016**, *2*, e1501856.

[7] S. Imani, A. J. Bandodkar, A. V. Mohan, R. Kumar, S. Yu, J. Wang, P. P. Mercier, *Nat. Commun.* **2016**, *7*, 11650.

[8] J. R. Corea, A. M. Flynn, B. Lechêne, G. Scott, G. D. Reed, P. J. Shin, M. Lustig, A. C. Arias, *Nat. Commun.* **2016**, *7*, 10839.

[9] S. L. Swisher, M. C. Lin, A. Liao, E. J. Leeflang, Y. Khan, F. J. Pavinatto, K. Mann, A. Naujokas, D. Young, S. Roy, M. R. Harrison, A. C. Arias, V. Subramanian, M. M. Maharbiz, *Nat. Commun.* **2015**, *6*, 6575.

[10] Y. Khan, F. J. Pavinatto, M. C. Lin, A. Liao, S. L. Swisher, K. Mann, V. Subramanian, M. M. Maharbiz, A. C. Arias, *Adv. Funct. Mater.* **2016**, *26*, 1004.

[11] S. Takamatsu, T. Lonjaret, E. Ismailova, A. Masuda, T. Itoh, G. G. Malliaras, *Adv. Mater.* **2016**, *28*, 4485.

[12] S. Choi, H. Lee, R. Ghaffari, T. Hyeon, D.-H. Kim, *Adv. Mater.* **2016**, *28*, 4203.

[13] M. Drack, I. Graz, T. Sekitani, T. Someya, M. Kaltenbrunner, S. Bauer, *Adv. Mater.* **2015**, *27*, 34.

[14] Q. Cao, H.-S. Kim, N. Pimparkar, J. P. Kulkarni, C. Wang, M. Shim, K. Roy, M. A. Alam, J. A. Rogers, *Nature* **2008**, *454*, 495.

[15] B. Crone, A. Dodabalapur, Y.-Y. Lin, R. Filas, Z. Bao, A. LaDuca, R. Sarpeshkar, H. Katz, W. Li, *Nature* **2000**, *403*, 521.

[16] Y. Khan, A. E. Ostfeld, C. M. Lochner, A. Pierre, A. C. Arias, *Adv. Mater.* **2016**, *28*, 4373.

[17] S. Park, Y. J. Kang, S. Majd, *Adv. Mater.* **2015**, *27*, 7583.

[18] Y. S. Rim, S.-H. Bae, H. Chen, N. De Marco, Y. Yang, *Adv. Mater.* **2016**, *28*, 4415.

[19] A. E. Ostfeld, A. M. Gaikwad, Y. Khan, A. C. Arias, *Sci. Rep.* **2016**, *6*, 26122.

[20] A. E. Ostfeld, I. Deckman, A. M. Gaikwad, C. M. Lochner, A. C. Arias, *Sci. Rep.* **2015**, *5*, 15959.

[21] A. C. Arias, J. D. MacKenzie, I. McCulloch, J. Rivnay, A. Salleo, *Chem. Rev.* **2010**, *110*, 3.

[22] J. A. Rogers, T. Someya, Y. Huang, *Science* **2010**, *327*, 1603.

[23] L. Pan, A. Chortos, G. Yu, Y. Wang, S. Isaacson, R. Allen, Y. Shi, R. Dauskardt, Z. Bao, *Nat. Commun.* **2014**, *5*, 3002.

[24] C.-C. Huang, Z.-K. Kao, Y.-C. Liao, *ACS Appl. Mater. Interfaces* **2013**, *5*, 12954.

[25] J. Webster, *Medical Instrumentation: Application and Design*, John Wiley & Sons, Hoboken, NJ **2010**.

[26] S. Xu, Y. Zhang, L. Jia, K. E. Mathewson, K.-I. Jang, J. Kim, H. Fu, X. Huang, P. Chava, R. Wang, S. Bhole, L. Wang, Y. J. Na, Y. Guan, M. Flavin, Z. Han, Y. Huang, J. A. Rogers, *Science* **2014**, *344*, 70.

[27] A. M. Gaikwad, A. C. Arias, D. A. Steingart, *Energy Technol.* **2015**, *3*, 305.

[28] M. Poliks, J. Turner, K. Ghose, Z. Jin, M. Garg, Q. Gui, A. Arias, Y. Kahn, M. Schadt, F. Egitto, *presented at IEEE 66th Electronic Components and Technology Conference (ECTC)*, June **2016**, Las Vegas, NV, USA, pp. 1623.